Shallow Convection and Buoyancy Equilibration in an Idealized Coastal Polynya*

DAVID C. CHAPMAN AND GLEN GAWARKIEWICZ

Woods Hole Oceanographic Institution, Woods Hole, Massachusetts

ABSTRACT

The recent theoretical approach of Visbeck, Marshall, and Jones is used to examine shallow convection and offshore transport of dense water from an idealized coastal polynya. A constant negative buoyancy flux is applied in a half-elliptical region adjacent to a coastal boundary, surrounded by a forcing decay region with uniform width W over which the imposed buoyancy flux decreases smoothly to zero. Initially, the density beneath the forcing increases linearly with time. A baroclinically unstable front forms at the edge of the forcing region. The width of the front is imposed by the width of the forcing decay region, provided this distance is larger than the baroclinic Rossby radius. Baroclinic eddies, whose velocities are inversely proportional to W, develop along the front and exchange dense water from the forcing region with ambient water, eventually reaching an equilibrium in which the lateral buoyancy flux by eddies balances the prescribed surface buoyancy flux. The time to reach equilibrium t_e and the equilibrium density anomaly ρ_e are given by

$$t_e = \beta\left(\frac{fWb}{B_0}\right)^{1/2}; \qquad \rho_e = \beta\frac{\rho_0}{gH}(fB_0Wb)^{1/2},$$

where B_0 is the imposed buoyancy flux, b the offshore width of the constant forcing region, H the water depth, f the Coriolis parameter, ρ_0 a reference density, and g the gravitational acceleration. Finally, $\beta = [\pi/2\alpha'E(1 - b^2/a^2)]^{1/2}$, where a is the length of the constant forcing region along the coast, α' is the efficiency of eddy exchange, and E is the complete elliptic integral of the second kind. These parameter dependencies are fundamentally different from previous results for deep or shallow convection (1/2 power rather than 1/3 or 2/3) owing to the influence of the forcing decay region. The scalings are confirmed with numerical calculations using a primitive equation model. Eddy exchange in shallow convection is several times more efficient than in open-ocean deep convection. Some implications for Arctic coastal polynyas are discussed.

1. Introduction

Recently, we used a numerical model to examine the formation and subsequent offshore transport of dense shelf water associated with a shallow coastal polynya (Gawarkiewicz and Chapman 1995, hereinafter GC). The effect of brine rejection accompanying ice formation within the polynya was idealized as a region of constant negative buoyancy forcing at the surface adjacent to a coastal boundary. The typical response to negative buoyancy forcing is as follows. The surface forcing increases the density of the water directly beneath it, which then mixes to the bottom (instantly in the hydrostatic model). For constant buoyancy forcing, the density within the forcing region increases linearly with time. A density front forms at the edge of the

forcing region, which then adjusts toward geostrophy, generating a cyclonic surface jet and an anticyclonic bottom jet along the front. The front is baroclinically unstable, so waves grow and eventually form eddies that move away from the front, transporting dense water offshore from the forcing region and replacing it with lighter ambient water. As a result, the density beneath the forcing region cannot continue to increase linearly with time, but rather reaches a maximum and remains fairly constant despite continued buoyancy forcing. That is, a nearly equilibrium state is reached in which the loss of buoyancy through the surface is balanced by the addition of lighter ambient water to the polynya by eddies.

This response to negative buoyancy forcing was found to be quite robust. The same basic sequence of events occurred for a wide range of model parameters. However, no theory was provided to explain the time scale for the onset of offshore eddy transport or the equilibrium density achieved beneath the forcing region as a function of the various model parameters.

The sequence of events described above is similar in many respects to the behavior in models of deep convection reported by, for example, Jones and Marshall

---

Corresponding author address: Dr. David C. Chapman, Woods Hole Oceanographic Institution, Woods Hole, MA 02543.
E-mail: dave@matt.whoi.edu

(1993), Maxworthy and Narimousa (1994), Ivey et al. (1995), Brickman (1995), Coates et al. (1995), and Whitehead et al. (1996). These studies have examined the response to negative surface buoyancy forcing (or the equivalent positive buoyancy forcing at the bottom) confined within an isolated region (typically a circular disk). As dense water descends beneath the forcing region, baroclinic eddies develop around the edge of the forcing region and exchange dense water from the forcing region with lighter ambient water. Eventually the eddy exchange balances the buoyancy reduction at the surface, and an equilibrium state is reached despite continued forcing.

To understand the dynamics of the equilibrium state, Visbeck et al. (1996, hereinafter VMJ) have cleverly applied the ideas of parcel theory to the energetics of deep convection in a stratified ocean. They considered the response to surface cooling in a circular region and assumed that a buoyancy equilibrium exists as described above; that is, baroclinic eddies carry buoyancy into the "chimney" beneath the forcing as fast as cooling removes buoyancy at the surface. A judicious choice of approximations and simplifications then produced the following scales for the time to reach equilibrium t_f, the final depth of the chimney h_f, and the equilibrium density anomaly within the chimney ρ_f:

$$t_f = \frac{\gamma^2}{2}\left(\frac{r^2}{B_0}\right)^{1/3}; \quad h_f = \gamma\frac{(B_0 r)^{1/3}}{N}; \quad \rho_f = \gamma\frac{\rho_0 N}{g}(B_0 r)^{1/3}, \tag{1}$$

where r is the radius of the cooling region, B_0 is the applied surface buoyancy flux (units of $m^2\ s^{-3}$), N is the initial buoyancy frequency, ρ_0 is a constant reference density, g is the acceleration due to gravity, and γ is a constant that is inversely related to the correlation between radial velocity variations and density variations. Basically, γ^{-1} is a measure of the efficiency with which the eddies transport buoyancy. VMJ showed that results from a variety of numerical and laboratory experiments are consistent with (1), and they estimated γ to be 3.9 $\pm$ 0.9.

VMJ also applied their theory to a weakly stratified ocean in which the chimney penetrates to the bottom. This may be understood by considering the initial deepening of the chimney, which follows the well-known one-dimensional theoretical result [which has recently been confirmed in laboratory experiments by Ivey et al. (1995)]

$$h = \frac{(2B_0 t)^{1/2}}{N}, \tag{2}$$

where h is the chimney depth and t is time [VMJ's Eq. (4)]. If the stratification is weak and/or the water is shallow, then the chimney may reach the bottom in a time less than t_f, so (1) no longer applies. For this shallow case, VMJ showed that the time to reach equilibrium

t_s and the equilibrium density anomaly ρ_s are given by

$$t_s = \gamma^2\left(\frac{r^2}{B_0}\right)^{1/3}; \quad \rho_s = \gamma^2\frac{\rho_0}{gH}(rB_0)^{2/3}, \tag{3}$$

where H is the total water depth.

In an attempt to understand the behavior of our shallow coastal polynya (GC), we applied (3) but found poor agreement. We then considered two possible reasons for the discrepancies. First, the presence of the coastal boundary may complicate the dynamics by allowing boundary-trapped motions (e.g., waves or steady currents) to carry dense water out of the forcing region in addition to transport by eddies. It is not obvious that the characterization of the eddies used by VMJ to obtain (3) will still apply. However, we found no evidence of boundary-trapped motions transporting significant amounts of dense water prior to reaching the equilibrium state (GC), so this explanation was discounted. The second possibility stems from the choice of length scales for the density front. In deriving both (1) and (3), VMJ assumed the horizontal scale of the density front to be the baroclinic Rossby radius; Nh_f/f for (1) and NH/f for (3). This assumption is reasonable provided that the baroclinic Rossby radius is the dominant horizontal length scale. Indeed, in VMJ and the other previously cited deep-convection studies, the imposed buoyancy forcing was spatially discontinuous, that is, uniform within the forcing region and vanishing outside the forcing region, so the baroclinic Rossby radius is the only possible horizontal length scale for the front. However, for weak stratification the baroclinic Rossby radius may be smaller than other length scales—for example, scales imposed by spatially varying buoyancy forcing, so the density front may be wider than the baroclinic Rossby radius. In our shallow coastal polynya calculations (GC), the forcing was gradually reduced to zero through a forcing decay region surrounding the uniform forcing region. The forcing decay region is intended to represent variations in ice concentration from a minimum within the coastal polynya to a maximum outside the polynya. In general, the length scale of the forcing decay region is determined by a combination of meteorological forcing and ice dynamics, for example, wind-driven ice accumulation or temporal variability in the position of the ice edge. If the scale of the forcing decay region is larger than the baroclinic Rossby radius, then (3) may not apply. This is the situation that we explore here.

We apply the approach and ideas of VMJ to shallow convection in the idealized coastal polynya considered by GC. A theory is developed in section 2 that accounts for the imposed length scale of the forcing decay region and produces new scales for the time to reach equilibrium and the equilibrium density anomaly. In section 3, numerical calculations are used to confirm these scales. The effects of a forcing decay region on deep-convection scales are briefly considered in section 4. The results are summarized and discussed in section 5.
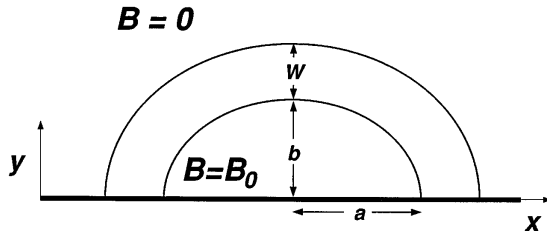
FIG. 1. Model geometry: uniform negative buoyancy forcing that decays to zero over a distance W, adjacent to a straight coast (x axis).

2. Theory

As in GC, we idealize the effect of brine rejection during ice formation within a coastal polynya by applying a negative surface buoyancy flux within a half-elliptical region adjacent to a straight coastal boundary (Fig. 1). The x axis is aligned with the coast, while the y axis points offshore. The buoyancy forcing is fixed at B_0 within the half-ellipse with principal axes a, b in the x, y directions, respectively. Surrounding this half-ellipse is a forcing decay region of width W in which the buoyancy flux decreases linearly to zero. Thus, the surface buoyancy flux is zero outside the larger half-ellipse with principal axes $a + W$ and $b + W$.[1] The forcing may be written as

$$B = \begin{cases} B_0, & r_i < 1 \\ B_0(1 - r_o)/(1 - r_o/r_i), & r_i > 1, r_o < 1 \\ 0, & r_o > 1, \end{cases}$$
(4)

where $r_i^2 = x^2/a^2 + y^2/b^2$ and $r_0^2 = x^2/(a + W)^2 + y^2/(b + W)^2$.

The ocean is assumed to begin at rest with constant density ρ_0 before the buoyancy forcing is applied at time $t = 0$. The ocean depth H is constant. Following VMJ, a quasi-steady state is assumed in which the buoyancy extracted from the surface is balanced by the eddy flux of buoyancy around the periphery of the forcing region:

$$\iint \frac{\rho_0}{g} B \, dA = \int_{-H}^{0} \oint \overline{v^n \rho} \, dl \, dz,$$
(5)

where v^n represents velocity perturbations normal to the edge of the forcing region, ρ is the density anomaly, A is the surface area, l is the distance along the edge of the forcing region, and z is the vertical coordinate; the overbar denotes a time average. For simplicity, we consider here only the buoyancy flux within the constant flux region (i.e., the inner half-ellipse where $B = B_0$ in Fig. 1). This choice produces simple parameter dependencies that are easily interpreted but limits the application to cases where b is comparable to or greater than W. The effect of the buoyancy flux over the forcing decay region is minor and is addressed in the appendix. As in VMJ, we also assume that $\overline{v^n \rho}$ is roughly independent of z and l, so (5) may be approximated by

$$\frac{\rho_0}{g} B_0 G(a,b) = \alpha H P(a,b) \overline{v^n \rho},$$
(6)

where α is a constant of proportionality (as in VMJ) that accounts for lateral variations in the eddy flux, $G(a, b)$ is the area of the buoyancy forcing region, and $P(a, b)$ is the perimeter of the forcing region. In the present case of a half-elliptical forcing region, $G(a, b) = \pi ab/2$ and $P(a, b) = 2aE(1 - b^2/a^2)$ where $E(\mu)$ is the complete elliptic integral of the second kind (Abramowitz and Stegun 1965). However, as written, (6) is valid for any spatially limited forcing region.

The general scenario is that a surface-to-bottom front forms along the edge of the forcing region. The front adjusts toward geostrophy before baroclinic instability sets in. We expect that the velocity within the eddies will, at least initially, be approximately equal to the geostrophic velocity along the front. The thermal wind balance implies

$$\frac{\partial v^n}{\partial z} \approx \frac{\partial v^a}{\partial z} = -\frac{g}{\rho_0 f} \frac{\partial \rho}{\partial n},$$

where v^a is the velocity along the edge of the forcing region, n is directed normal to the edge of the forcing region, and f is the (constant) Coriolis parameter. This is consistent with VMJ, who found that parcel theory leads to velocity and density fluctuations that are in thermal wind balance. The surface and bottom frontal velocities are nearly equal and opposite (GC), so $\partial v^n/\partial z \approx 2v^n/H$. The horizontal scale of the density front depends on the relative sizes of the baroclinic Rossby radius, $R = (g\rho H/\rho_0)^{1/2}/f$, and the imposed length scale W. From GC, the maximum baroclinic Rossby radius achieved during the numerical calculations is typically quite small, less than 5 km. Therefore, for $W \gtrsim 5$ km, W should set the horizontal scale in the thermal wind balance ($\partial \rho/\partial n \approx -\rho/W$) to obtain

$$v^n \approx \frac{gH\rho}{2\rho_0 fW}.$$
(7)

Substitution of (7) and the definitions of G and P into (6) yields

$$\frac{\rho_0}{g} \frac{\pi ab}{2} B_0 = \alpha' \frac{gH^2}{2\rho_0 fW} 2aE(1 - b^2/a^2) \overline{\rho^2},$$
(8)

where α' is a new proportionality constant that accounts for both the spatial variations in eddy flux and the imperfect correlation between v^n and ρ. Equation (8) can be rearranged to provide an estimate for the equilibrium density anomaly

---

[1] GC used a slightly different forcing decay region; a cosine taper whose width varied around the edge of the half-elliptical forcing region (see their Fig. 1). A region of uniform width with a linear decrease in forcing is simpler for the present purposes, although conceptually there is no difference. Eddy formation and transport are qualitatively the same for both forcing functions.

$$\rho_e = \beta \frac{\rho_0}{gH}(fB_0Wb)^{1/2}, \qquad (9)$$

where $\beta = [\pi/2\alpha'E(1 - b^2/a^2)]^{1/2}$.

According to (2), the time required for the dense water to reach the bottom should be $t_b = N^2H^2/2B_0$. Obviously, $t_b = 0$ when $N = 0$, as assumed here. More generally, if N is small enough that $t_bf \ll 1$, then the dense water essentially reaches the bottom instantly, mixing with and increasing the density of the entire water column. Consequently, the density anomaly beneath the forcing region initially increases linearly with time (GC, VMJ) as

$$\rho = \frac{\rho_0 B_0 t}{gH}. \qquad (10)$$

Combining (9) and (10) produces an estimate for the time to reach equilibrium

$$t_e = \beta \left(\frac{fWb}{B_0}\right)^{1/2}. \qquad (11)$$

It is important to recognize immediately the fundamental difference in parameter dependence between (9), (11), and (3). That is, the exponents in (9) and (11) for both t_e and ρ_e are 1/2 whereas the exponents in (3) are 1/3 for t_s and 2/3 for ρ_s. This indicates that, relative to VMJ's results, the shallow coastal polynya has a weaker dependence on buoyancy forcing B_0 but a stronger dependence on the size of the forcing region b. [Note that b is analogous to r in (3). They are identical for a circular forcing region, for which $a = b = r$ and $E(0) = \pi/2$.] The behavioral difference stems from the choice of horizontal length scale in the thermal wind balance (7). We chose W for this scale, but if W were replaced in (7) by the baroclinic Rossby radius, R, then the equivalent of (3), applied to a half-elliptical forcing region, would be recovered. In the next section, scalings (9) and (11) are tested using numerical calculations like those of GC.

3. Numerical calculations

a. Model description

The numerical calculations used to test the parameter dependencies (9) and (11) are only slightly modified from those of GC. We use the semispectral primitive equation model (SPEM), described in detail by Haidvogel et al. (1991), to solve the following hydrostatic and Boussinesq momentum, density, and continuity equations:

$$u_t + uu_x + vu_y + wu_z - fv = -\frac{1}{\rho_0} p_x + (A_V u_z)_z + F_u \quad (12)$$

$$v_t + uv_x + vv_y + wv_z + fu = -\frac{1}{\rho_0} p_y + (A_V v_z)_z + F_v \quad (13)$$

$$p_z = -\rho g \qquad (14)$$

$$\rho_t + u\rho_x + v\rho_y + w\rho_z = (K_V \rho_z)_z + F_\rho \qquad (15)$$

$$u_x + v_y + w_z = 0. \qquad (16)$$

In this system (u, v, w) represent the (x, y, z) components of the velocity, p is the pressure, A_V is the vertical eddy viscosity, K_V is the vertical eddy diffusivity, and ρ, ρ_0, f, g, and t have been previously defined. The variables $F_{u,v,\rho}$ represent dissipative functions that are required for numerical stability. Subscripts $x, y, z,$ and t denote partial differentiation.

The system (12)–(16) is approximated using finite differences in the horizontal, a stretched vertical (sigma) coordinate to handle variations in the bottom topography, and a high-order spectral approximation (an expansion in modified Chebyshev polynomials) to represent the vertical flow structure. A leapfrog-trapezoidal time-stepping scheme is used with an occasional trapezoidal step correction. Haidvogel et al. (1991) give further model details.

The model domain is a high-latitude, uniformly rotating ($f = 1.3 \times 10^{-4}$ s^{-1}), straight channel with a coastal wall at $y = 0$ and an offshore (solid) wall at $y = 75$ km. The channel is 150 km long with periodic boundaries at the ends ($x = -75$ km and $x = 75$ km). The channel is wide enough and long enough so that the boundaries do not significantly influence the evolution of the dense water during the time of interest here. The ocean has constant depth $H = 50$ m. There is no flow through the bottom, and a rigid lid is assumed at the surface (i.e., $w = 0$ at $z = 0$). The numerical grid is uniform in the horizontal with 74 along-channel and 37 across-channel grid points; that is, $\Delta x = \Delta y = 2.08$ km. This is about half the resolution of GC's calculations, however, comparisons with finer resolution show only minor differences. Nine Chebyshev polynomials are used to resolve the vertical structure. The model time step is 288 s.

Both surface and bottom stress are set to zero: $A_V u_z = A_V v_z = 0$ at $z = 0, -H$. Buoyancy forcing is applied by setting $K_V \rho_z = \rho_0 B/g$ at the surface, where B is given by (4). There is no density flux through the bottom: $K_V \rho_z = 0$ at $z = -H$. Typical lengths for the forcing region are $a = 30$ km, $b = 10$ km, and $W = 10$ km. These will, of course, be changed to test (9) and (11). The maximum buoyancy flux ranges from $B_0 = 1 \times 10^{-7}$ to 16×10^{-7} m^2 s^{-3}. (B can be converted to a density flux as $Q = \rho_0 B/g$.) For comparison, the seasonally averaged haline buoyancy flux in polynya zones within the western Arctic is estimated to be 2.7×10^{-7} m^2 s^{-3} (Cavalieri and Martin 1994).

As in GC, the vertical mixing coefficients are approximated using a Richardson-number-dependent scheme:

$$A_V = 0.0001 + \frac{0.0049}{(1 + 0.3\text{Ri})^{1/2}} \qquad (17)$$

$$K_V = 0.0001 + \frac{0.0049}{(1 + 0.3\text{Ri})^{3/2}}, \qquad (18)$$

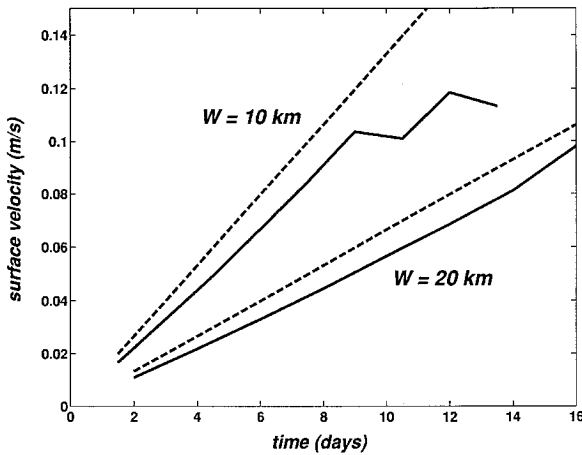where the units are meters squared per second and the Richardson number is defined by

FIG. 2. Maximum surface velocity in the frontal region versus time for $W = 10$ and 20 km (solid curves). Other model parameters are set at $B_0 = 4 \times 10^{-7}$ m^2 s^{-3}, $a = 30$ km, $b = 10$ km, and $H = 50$ m. Geostrophic estimates from (7) are shown for comparison (dashed curves).

FIG. 3. Average density anomaly in the forcing region as a function of time for various buoyancy fluxes, $B_0 = 1, 2, 4, 8,$ and 16 ($\times 10^{-7}$ m^2 s^{-3}) and other parameters set at $a = 30$ km, $b = 10$ km, $W = 10$ km, and $H = 50$ m. The dashed lines represent the linear increase in ρ with time given by (10) for each case.

$$\text{Ri} = \frac{-g\rho_z/\rho_0}{(u_z)^2 + (v_z)^2}. \quad (19)$$

Additional vertical mixing of density is applied in the form of instantaneous vertical convective adjustment whenever the water column becomes statically unstable (i.e., when lighter water appears under heavier water). Lateral diffusion of both momentum and density is necessary for numerical stability. We apply Laplacian subgrid-scale mixing with constant mixing coefficients (i.e., $F_{u,v} = \nu_u \nabla^2 u, v; F_\rho = \nu_\rho \nabla^2 \rho$) while using the smallest mixing coefficients allowable, $\nu_u = 50$ m^2 s^{-1} and $\nu_\rho = 5$ m^2 s^{-1}.

Each calculation begins from rest. The fluid in the channel is initially homogeneous with $\rho = 0$. At time $t = 0$, the surface buoyancy flux is applied and held fixed for a time equivalent to $2t_e$ for the particular parameter choices, typically between 7 and 40 days of simulation time.

b. Testing the scales

To test (9) and (11), we have made numerous numerical calculations with different combinations of B_0, a, b, W, and H. We have not varied ρ_0 ($= 1000$ kg m^{-3}) or f because they typically change by only a small fraction in the ocean (limiting ourselves to mid and higher latitudes for f), whereas the other parameters may easily change by a factor of 2 or more.

We first tested our assumption that the width of the forcing decay region determines the horizontal scale of the frontal density gradient and, hence, the alongfront geostrophic velocity used to estimate v^n. Figure 2 shows the maximum surface velocity in the frontal region as a function of time for two choices of forcing decay width, $W = 10$ and 20 km (solid curves) along with the
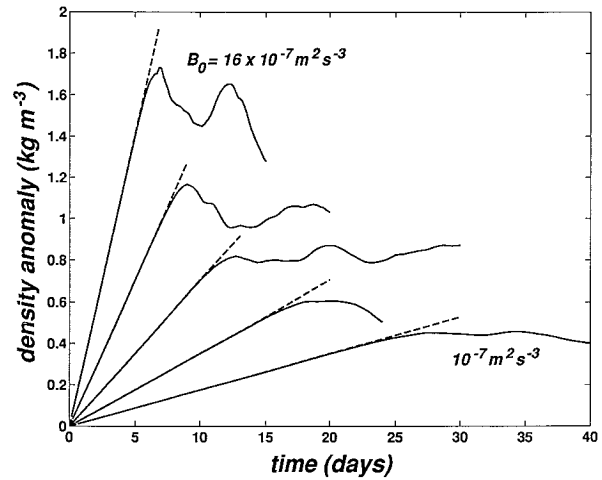
geostrophic estimate (7) (dashed curves). Other parameters are set at $B_0 = 4 \times 10^{-7}$ m^2 s^{-3}, $a = 30$ km, $b = 10$ km, and $H = 50$ m. In both cases, the model velocity closely follows the geostrophic estimate but is slightly weaker because of the small horizontal viscosity in the numerical calculations, which smooths the flow fields a bit. Nevertheless, the model velocities are clearly proportional to W^{-1} as assumed, and (7) provides a good estimate for v^n until eddy exchange begins (about day 9 for $W = 10$ km).

The clearest and perhaps most convincing test of (9) and (11) is to vary the buoyancy flux B_0 because this tests the square root dependence in (9) and (11) without the complication of altering β. Figure 3 shows the density anomaly within the forcing region (averaged over an area extending 4 km from the coast and stretching 42 km along the coast) as a function of time for buoyancy fluxes ranging from $B_0 = 1 \times 10^{-7}$ to 16×10^{-7} m^2 s^{-3}. Other parameters are fixed at $a = 30$ km, $b = 10$ km, $W = 10$ km, and $H = 50$ m. As expected, the qualitative behavior is identical in each case. Initially, the density anomaly increases linearly with time (dashed lines), consistent with (10). When baroclinic eddies begin transporting dense water offshore, the density anomaly breaks away from the linear increase and then varies about a quasi-steady value.

Figure 4 shows the same results as in Fig. 3, after scaling both time and density anomaly based on (9) and (11):

$$\tilde{t} = t\left(\frac{B_0}{fWb}\right)^{1/2}; \qquad \tilde{\rho} = \rho\left(\frac{gH}{\rho_0}\right)(fB_0Wb)^{-1/2}.$$

The curves overlay fairly closely, especially where they break away from the linear increase of density anomaly
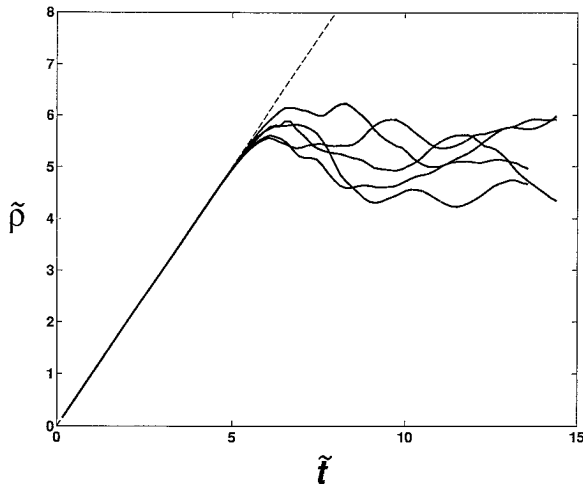
FIG. 4. As in Fig. 3 but after scaling both time and density anomaly based on (9) and (11): $\tilde{t} = t(B_0/fWb)^{1/2}$ and $\tilde{\rho} = \rho(gH/\rho_0)(fB_0Wb)^{-1/2}$. The dashed line represents a linear increase in $\tilde{\rho}$ with $\tilde{t}$.

with time. There is indeed some variability, which increases for $\tilde{t} \gtrsim 7$, but Fig. 4 indicates that the dependence on B_0 in (9) and (11) is correct.

For comparison, Fig. 5 also shows the results from Fig. 3, but after applying the VMJ scales (3) with b replacing r:

$$\tilde{t}_s = t\left(\frac{B_0}{b^2}\right)^{1/3}; \qquad \tilde{\rho}_s = \rho\left(\frac{gH}{\rho_0}\right)(B_0b)^{-2/3}.$$

The curves clearly do not overlay as well as in Fig. 4. The equilibrium densities vary by about 100%, confirming that the new scalings leading to (9) and (11) are more appropriate for cases in which the forcing decay region is larger than the baroclinic Rossby radius.
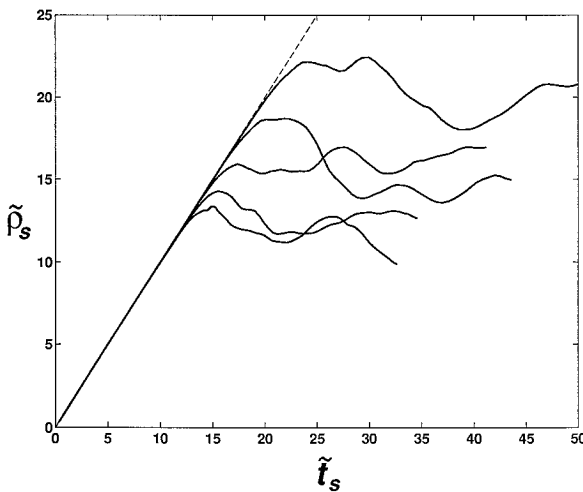

FIG. 5. As in Fig. 4 but using the VMJ scalings: $\tilde{t}_s = t(B_0/b^2)^{1/3}$ and $\tilde{\rho}_s = \rho(gH/\rho_0)(B_0b)^{-2/3}$. Note that the axes have different scales than in Fig. 4.
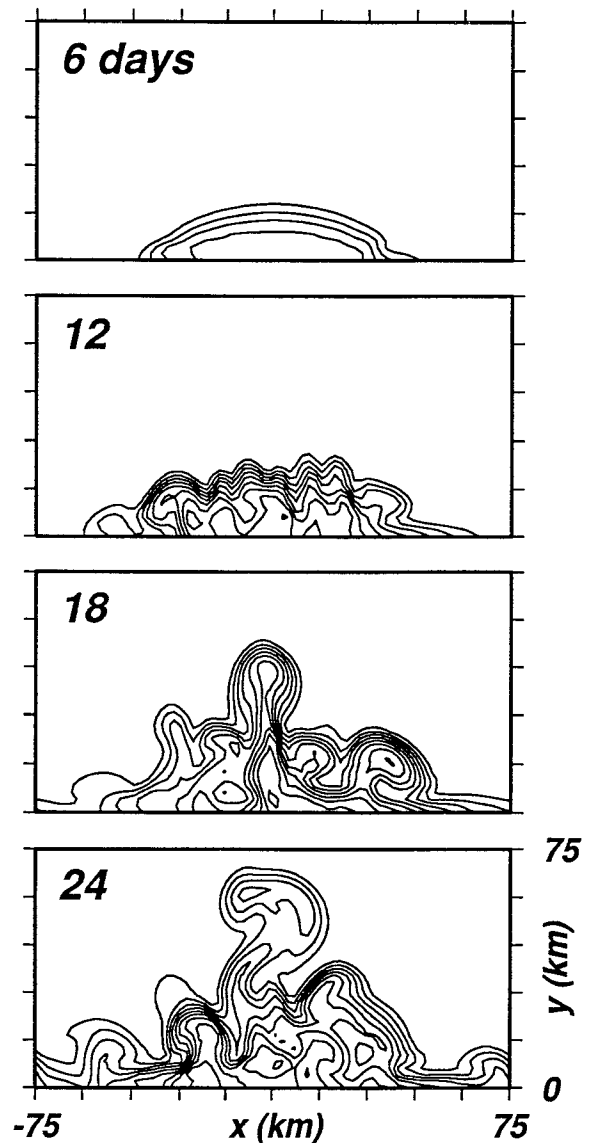

FIG. 6. Plan views of density anomaly at the bottom at various times for intermediate buoyancy forcing $B_0 = 4 \times 10^{-7}$ m^2 s^{-3} and other parameters set at $a = 30$ km, $b = 10$ km, $W = 10$ km, and $H = 50$ m. Contours are 0.1 to 1.0 by 0.1 kg m^{-3}.

The scaled equilibrium density anomaly in Fig. 4 is equal to β and can be estimated by averaging $\tilde{\rho}$ for $6 \leq \tilde{t} \leq 7$ to obtain $\beta = 5.7$ with an estimated uncertainty of about ± 0.2. From the definition of β, this implies that the eddy exchange efficiency is (with $b/a = 1/3$)

$$\alpha' = \pi/2\beta^2E(1 - b^2/a^2) = 0.043.$$

The variability in $\tilde{\rho}$ at larger $\tilde{t}$ results from the presence of only a small number of baroclinic eddies and their interactions. That is, only about four to five eddies form along the front at the edge of the forcing region (e.g., Fig. 6), so each eddy must carry a large fraction of the buoyancy to be exchanged in the equilibrium. Thus, the
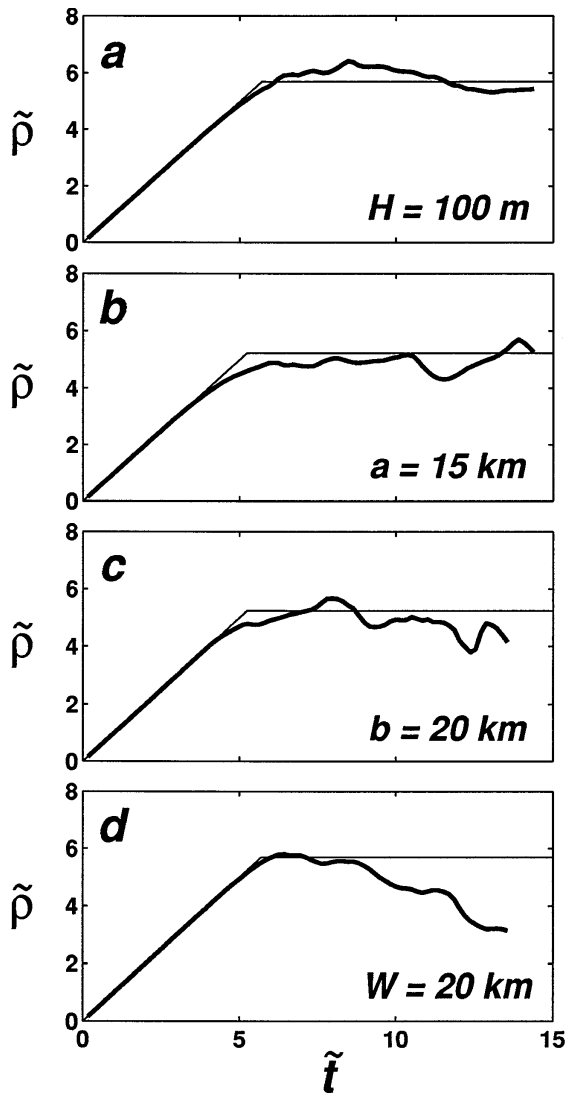
FIG. 7. Scaled density anomaly $\tilde{\rho}$ versus scaled time $\tilde{t}$ for various combinations of parameters. In each panel, the standard parameters ($B_0 = 4 \times 10^{-7}$ m² s⁻³, $a = 30$ km, $b = 10$ km, $W = 10$ km, and $H = 50$ m) are used except for the parameter noted. The thin solid line represents a linear increase in $\tilde{\rho}$ until equilibrium at $\tilde{\rho} = \beta$, where β is estimated in each case using $\alpha' = 0.043$ (based on Fig. 4 and the definition of β). In (a) and (d), $\beta = 5.7$; in (b) and (c), $\beta = 5.2$.

balance in (5) is approximate at any given time, depending on the details of the eddy field. This kind of eddy variability (between calculations or within a single model run) can, therefore, lead to temporal changes in the density anomaly within the forcing region. In other words, a statistical equilibrium is poorly approximated with so few eddies. In light of this, the degree to which the curves overlay in Fig. 4 is remarkable.

Variations of the other parameters are now considered individually and the results compared in Fig. 7 to the expected equilibrium behavior (thin line), that is, linear increase in $\tilde{\rho}$ with $\tilde{t}$ until $\tilde{\rho} = \beta$. In each case, β is

estimated by assuming that the eddy exchange efficiency α' is independent of model parameters.

The simplest parameter dependence occurs for the water depth H. According to (11), the time to reach equilibrium is unaffected by H, while the equilibrium density anomaly in (9) is inversely proportional to H. The coefficient β is independent of H, so $\beta = 5.7$. Figure 7a shows the result for a deeper shelf, $H = 100$ m, with the standard parameters: $a = 30$ km, $b = 10$ km, $W = 10$ km, and $B_0 = 4 \times 10^{-7}$ m² s⁻³. The scaled density anomaly follows close to the expected result with small variations at larger $\tilde{t}$, clearly verifying the parameter dependence.

The length of the forcing region a appears in (9) and (11) only within the argument of the elliptic integral in β. Furthermore, for $a \geq b$, the argument of the elliptic integral varies between 0 and 1, for which E varies between $\pi/2$ and 1. This implies a maximum possible change in β of about 25%. Figure 7b shows the response for a shorter forcing region, $a = 15$ km, and otherwise standard parameters: $b = 10$ km, $W = 10$ km, $H = 50$ m, and $B_0 = 4 \times 10^{-7}$ m² s⁻³. For $a = 15$ km, E increases by 18%, so the expected equilibrium occurs at $\beta = 5.2$. The close agreement with the expected result verifies the dependence of t_e and ρ_e on a through β in (9) and (11).

The offshore extent of the forcing region b appears in (9) and (11) both within the square roots and in the argument of E in β. Figure 7c shows the response for a wider forcing region, $b = 20$ km, and otherwise standard parameters: $a = 30$ km, $W = 10$ km, $H = 50$ m, and $B_0 = 4 \times 10^{-7}$ m² s⁻³. For this choice, the aspect ratio of the forcing region b/a is identical to the shorter polynya case (Fig. 7b), so E again increases by 18% over the standard case, yielding $\beta = 5.2$. Figure 7c shows that the dependence in (9) and (11) is correct.

Finally, Fig. 7d shows the response for a wider forcing decay region, $W = 20$ km.[2] Other parameters are set at $a = 30$ km, $b = 10$ km, $H = 50$ m, and $B_0 = 4 \times 10^{-7}$ m² s⁻³. The coefficient β is independent of W, so $\beta = 5.7$. The scaled density anomaly follows the expected result nearly perfectly for $\tilde{t} \leq 7$, again verifying (9) and (11). The decrease in $\tilde{\rho}$ at larger $\tilde{t}$ occurs when the eddies reach the boundaries of the longer model domain and does not represent a fundamental change in eddy behavior.

The agreement in Fig. 7d is particularly useful for validating the new estimates (9) and (11) and thereby the importance of W, because the VMJ scales are independent of W. That is, according to (9) and (11), doubling W produces a 41% increase in both ρ_e and t_e, whereas the VMJ scales, being independent of W, pre-

[2] With $W = 20$ km the eddies reach the periodic boundaries of the standard model domain before the equilibrium state is reached. Therefore, we extended the model domain to 200 km for this calculation, while keeping the same horizontal resolution.

dict no change in either ρ_e or t_e. Therefore, Fig. 7d shows clearly that (9) and (11) are more appropriate for the present configuration.

4. Deep convection with a forcing decay region

Our primary interest here is the dynamics of shallow convection, but the ideas introduced in section 2 can also be applied to the problem of deep convection. In particular, new scalings can be derived using the approach of VMJ, but now considering a circular forcing region that is surrounded by a forcing decay region whose width W is larger than the baroclinic Rossby radius.

We start with (6) and take $a = b$, so $G = \pi b^2$ and $P = 2\pi b$. For deep convection, the eddy flux occurs over the depth of the chimney h rather than the total water depth H, so (6) becomes

$$\frac{\rho_0}{g}B_0 b = 2\alpha h \overline{v^n \rho}. \tag{20}$$

The density at the base of the chimney is given by the definition of the buoyancy frequency

$$\rho = \rho_0 N^2 h/g, \tag{21}$$

and h increases in time according to (2). The geostrophic velocity is estimated from the thermal wind balance *within the forcing decay region,* where the depth of convective penetration depends on the local buoyancy forcing. That is, the *local* chimney depth is

$$h^\ell = \frac{(2Bt)^{1/2}}{N}, \tag{22}$$

where $B = B_0(b + W - r)/W$; that is, B decreases linearly with radius r from $B = B_0$ at $r = b$ to $B = 0$ at $r = b + W$. The geostrophic velocity may then be approximated as

$$v^n \approx -\frac{gh^\ell}{2\rho_0 f}\frac{\partial \rho^\ell}{\partial r} = -\frac{N^2 h^\ell}{2f}\frac{\partial h^\ell}{\partial r}, \tag{23}$$

where (21) has been applied locally. Substitution of (22) into (23) produces

$$v^n \approx \frac{B_0 t}{2fW}, \tag{24}$$

which can then be substituted into (20), along with (21) and (2), to obtain an estimate for the time to reach equilibrium

$$t_d = \frac{\gamma_d^2}{2}\left(\frac{fWb}{B_0}\right)^{1/2}, \tag{25}$$

where $\gamma_d = (2/\alpha')^{1/4}$. Equation (25) can be used with (2) and (21) to provide estimates of the equilibrium density and chimney depth:

$$\rho_d = \gamma_d \frac{\rho_0 N}{g}(fB_0 Wb)^{1/4}; \quad h_d = \gamma_d \frac{(fB_0 Wb)^{1/4}}{N}. \tag{26}$$

The primary effect of the forcing decay region is analogous to the shallow convection case; the dependence of the equilibrium quantities on B_0 and b is weakened relative to (1), and W is introduced into the scaling. We have made one numerical calculation of deep convection with a forcing decay region, which verifies both (2) and (24), but we have not made a systematic study of the parameter dependencies. Indeed, a detailed examination of the implications of the changes in the equilibrium scales is beyond the scope of this paper, but the results suggest that spatial variations in atmospheric forcing may play an important role in deep-convection processes and should be explored in future studies.

5. Summary and discussion

The numerical calculations described in section 3 strongly support the theory developed in section 2, which produced the relationships (9) and (11). The basic dynamics assumed by VMJ for open-ocean deep convection also apply to the case of a shallow coastal polynya despite the presence of the coastal boundary. That is, a constant negative surface buoyancy flux applied over a spatially limited region eventually leads to buoyancy equilibration in which baroclinic eddies exchange dense water with ambient water efficiently enough to balance the surface flux. However, there is one important difference. The horizontal scale of the density front generated around the edge of the shallow coastal polynya appears to be determined by the spatial scale of variability of the buoyancy forcing and not the baroclinic Rossby radius. In the present case, this scale is the width of the forcing decay region over which the buoyancy forcing vanishes. This single change from VMJ's theory produces a fundamental difference in the dependence of the equilibrium state on the various model parameters; that is, square root dependence rather than 1/3 and 2/3 powers [compare (9) and (11) with (3)].

Two conditions must be met for (9) and (11) to apply. First, the forcing decay scale must be larger than the baroclinic Rossby radius. Otherwise, the front will slump during geostrophic adjustment to the scale of the baroclinic Rossby radius. For example, the laboratory experiments of Maxworthy and Narimousa (1994), Ivey et al. (1995), Brickman (1995), Coates et al. (1995), and Whitehead et al. and the numerical calculations of Jones and Marshall (1993) all used a vanishingly small forcing decay region, so the frontal width was naturally the baroclinic Rossby radius. In each case, the behavior was consistent with the analysis of VMJ rather than (9) and (11). In contrast, we always choose W larger than the baroclinic Rossby radius in the shallow coastal polynya, consistent with (9) and (11). Second, the water must be shallow enough that rotation does not play a role in the sinking of dense plumes. That is, the dense water formed by the buoyancy forcing must sink to the bottom very rapidly. A measure of the importance of rotation during

sinking is the natural Rossby number, defined by Max-worthy and Narimousa (1994) as

$$\text{Ro*} = \left(\frac{B_0}{H^2 f^3}\right)^{1/2} = \frac{l_{\text{rot}}}{H}.$$

Here l_{rot} is the length scale over which rotation becomes important in the sinking convective cells (Jones and Marshall 1993). Rotation is important when Ro* < 1. Most studies of convection, including those cited above, consider cases with Ro* ≪ 1 with only a few cases in which Ro* approaches one. On the other hand, the shallow coastal polynya calculations presented here cover the range 2 < Ro* < 17, so rotation has little effect during the sinking process and (9) and (11) should apply.

On Arctic shelves the baroclinic Rossby radius is typically only a few kilometers, usually smaller than the scales of variability in forcing. Arctic shelves are also shallow enough that Ro* > 1 in a typical coastal polynya, so dense water should sink to the bottom rapidly. Together these imply that (9) and (11) may provide a reasonable description of the response in Arctic coastal polynyas and are probably more appropriate than (3). Thus, the forcing decay region, or ice concentration gradient region, is of fundamental importance in the dynamics of the flow field that develops, and its scale affects the timescale over which eddies develop as well as the equilibrium density anomaly attained.

The parameter dependencies in (9) and (11) can be understood on physical grounds. For example, stronger buoyancy forcing (larger B_0) leads to a faster increase in density anomaly, producing a larger density anomaly by the time equilibrium is reached, so t_e decreases while ρ_e increases. A deeper shelf (larger H) means a slower increase in density but also weaker geostrophic currents and, hence, weaker eddy velocities. These effects compensate so that t_e is unaffected. If t_e is unchanged, then ρ_e must decrease because the same buoyancy change is mixed over a greater depth. Both t_e and ρ_e are strongly dependent on the width of the forcing region b, but nearly independent of the length of the forcing region a, which only minimally changes the elliptic integral and hence β. This is reasonable because the equilibrium is reached by the *cross-shelf* exchange of dense water with ambient water; that is, eddy exchange must redistribute water across the entire polynya to the coast before an equilibrium can be achieved. Therefore, a wider forcing region (larger b) represents a greater cross-shelf distance for exchange, so it takes longer to reach equilibrium and both t_e and ρ_e increase. On the other hand, the length of the forcing region does not alter the cross-shelf exchange as long as eddies form along the entire length of the forcing region, so t_e and ρ_e are hardly affected. Finally, a wider forcing decay region (larger W) implies weaker horizontal density gradients introduced by the forcing. This leads to weaker geostrophic velocities and subsequently slower exchange by the eddies, thereby increasing both t_e and ρ_e.
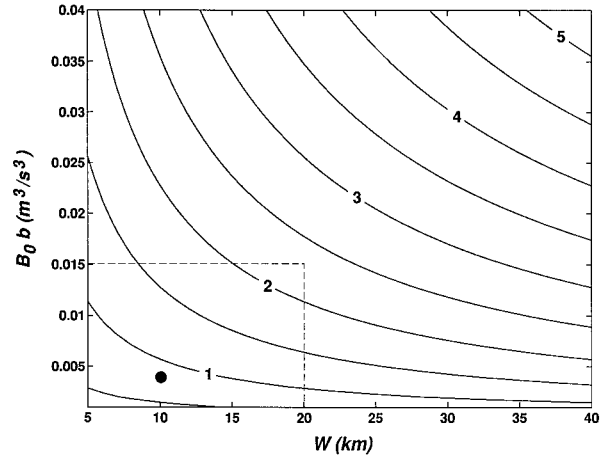

FIG. 8. Contours of ρ_e from (9) over a range of $B_0 b$ and W with β = 5.7, H = 50 m, ρ_0 = 1000 kg m^{-3}, and f = 1.3 × 10^{-4} s^{-1}. The thin dashed box in the lower left encloses values typical of Arctic coastal polynyas. The solid dot shows the standard parameter choices (B_0 = 4 × 10^{-7} m^2 s^{-3}, a = 30 km, b = 10 km, and W = 10 km).

The standard parameters used here are loosely based on observed values over Arctic shelves. The range of B_0 considered includes the mean value reported by Cavalieri and Martin (1994) for the western Arctic, B_0 = 2.7 × 10^{-7} m^2 s^{-3}, corresponding to a heat loss of 500 W m^{-2} from the polynya waters to the atmosphere. The polynya length scales (H, a, b, and W) are based on estimates from Pease (1987) and Schumacher et al. (1983). Using the standard parameters in (9) and (11), and β = 5.7 estimated from Fig. 4, suggests that the seasonally averaged buoyancy flux produces a maximum density anomaly of ρ_e = 0.69 kg m^{-3} after t_e = 14.5 days. An estimate of the interannual variation in B_0, based on nine years of data from Cavalieri and Martin (1994), suggests that salt production accompanying ice formation within polynyas of the western Arctic varies by roughly 15%. Individual regions may experience variations as large as 50% of the mean. From (9), a 50% change in B_0 produces only a 22% change in ρ_e. On synoptic times scales, the local buoyancy flux may be as much as three times the seasonal average (e.g., Cavalieri and Martin 1994), increasing ρ_e to 1.2 kg m^{-3}. The time to reach equilibrium decreases to 8.4 days, which is not inconsistent with some events reported by Cavalieri and Martin (1994; see, e.g., their Fig. 4). These estimates of ρ_e also fall close to the range of density anomalies associated with observed salinity elevations reported by Cavalieri and Martin (1994), which range from 1 to 2 psu, or 0.8 to 1.6 kg m^{-3}. Of course, the sensitivity of the equilibrium density anomaly to the water depth H makes these estimates rather approximate.

Figure 8 summarizes the dependence of ρ_e on the model parameters. The axes cover extreme values of the parameters showing the wide range of possible density anomalies, but typical values are found in the lower left corner ($B_0 b$ ≤ 0.015 m^3 s^{-3}, W ≤ 20 km), ranging from

0.5 to 2 kg m^{-3}. It is important to remember that the strongest parameter dependence in (9) occurs for the water depth because $\rho_e \propto 1/H$. That is, the values in Fig. 8 would double if the coastal polynya were over a shelf 25 m deep, in which case the seasonally averaged forcing defined above would produce a density anomaly of $\rho_e = 1.38$ kg m^{-3}. This sensitivity to water depth, coupled with the fact that many Arctic shelves are quite shallow over large offshore distances relative to the polynya scale b, suggests that regional differences in geomorphology may play an important role in the production of dense water masses. The sensitivity to the forcing decay scale is also important, with ρ_e doubling for an increase in W from 10 to 40 km. However, this scale has not been closely examined in observations and bears further investigation.

One conclusion from Fig. 8 is that typical variations in the buoyancy flux apparently do not have a large effect on the maximum density anomaly of water formed in a coastal polynya. This implies that dense water production from coastal polynyas may depend more on the ambient density of shelf water when the freezing season begins than on the surface buoyancy flux. This is consistent with Melling's (1993) conclusion that the interannual variability in dense water production over the Mackenzie Shelf is strongly influenced by variations in the autumn salinities before freezing begins. According to our scaling, if autumn salinities near the coast are lower than the mid and outer shelf densities by enough to decrease the density by 0.5–1.0 kg m^{-3}, then typical surface buoyancy fluxes due to brine rejection may be insufficient to raise the density beyond the midshelf values. Thus, dense water formation may be inhibited for that entire season, perhaps partially explaining the intermittency of dense water observations.

The equilibrium density anomaly (9) can be used to estimate typical velocities within the baroclinic eddies as well as the maximum baroclinic Rossby radius. From (7),

$$v^n \approx \frac{\beta}{2}\left(\frac{B_0 b}{fW}\right)^{1/2} \qquad (27)$$

which, for the standard parameters, yields a reasonable value of 0.11 m s^{-1}. Using (9), the baroclinic Rossby radius at equilibrium is

$$R_e = \left(\frac{g\rho_e H}{\rho_0 f^2}\right)^{1/2} = \beta^{1/2}\left(\frac{B_0 W b}{f^3}\right)^{1/4}. \qquad (28)$$

For the standard parameters, $R_e = 4.9$ km. More importantly, the baroclinic Rossby radius is rather insensitive to the model parameters, changing only as the 1/4 power, so it is unlikely to become much larger than about 5 km. Even a factor of 10 increase in B_0, W, or b would only increase R_e to 8.7 km. The implication is that the forcing decay scale is likely to be larger than the baroclinic Rossby radius regardless of the sizes of the other parameters. This supports the idea that spatial variations in the forcing probably determine the hori-
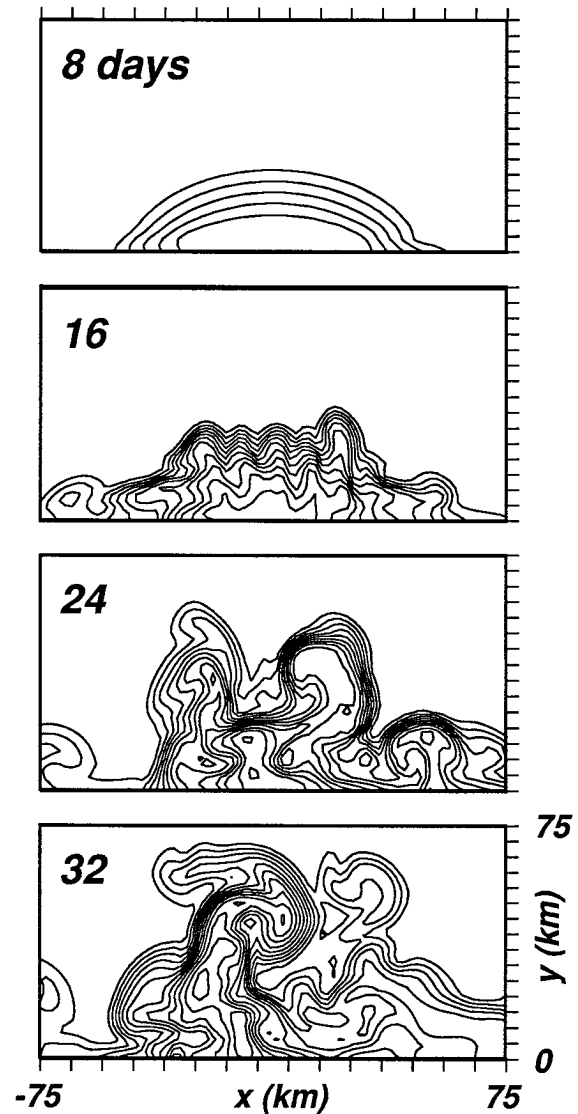

FIG. 9. As in Fig. 6 but with $W = 20$ km. Contours are 0.1 to 1.4 by 0.1 kg m^{-3}.

zontal scale for density variations in Arctic polynyas, and not the baroclinic Rossby radius. Interestingly, the baroclinic Rossby radius appears to determine the size of the eddies produced by the frontal instability. Figure 9 shows contours of density anomaly at the bottom for $W = 20$ km and otherwise standard parameters. Times are chosen to be nearly equivalent in scaled units to those in Fig. 6. The initial size of the growing eddies is quite similar for both cases, although nonlinear processes tend ultimately to produce somewhat larger eddies for $W = 20$ km. Thus, (28) suggests that the size of eddies over Arctic shelves should be fairly uniform with diameters in the range 20–25 km, consistent with our numerical calculations as well as observations (e.g., Manley and Hunkins 1985).
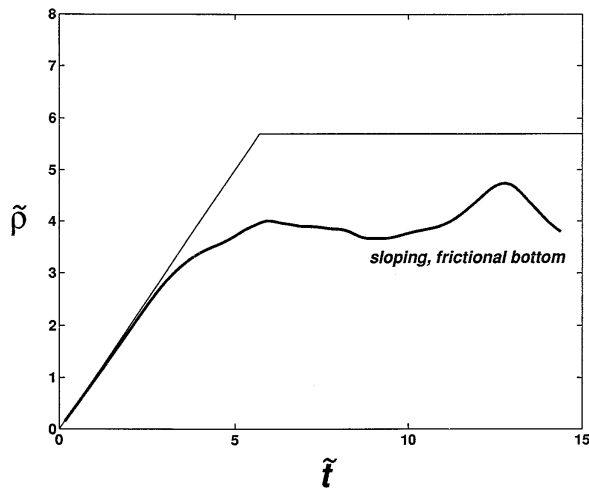
VMJ estimated the efficiency of eddy exchange α'

FIG. 10. As in Fig. 7, using the standard parameters (B_0 = 4 × 10^{-7} m^2 s^{-3}, a = 30 km, b = 10 km, W = 10 km, and H = 50 m) but over a uniformly sloping shelf with linear bottom friction.

for open-ocean deep convection to be about the same as that previously estimated for the atmosphere; α' = 0.008 ± 0.005. For our shallow coastal polynya calculations, the eddy exchange efficiency was found to be α' = 0.043. This is more than five times the efficiency of the deep-convection eddies, implying that the shallow coastal polynya is generally a more efficient place to exchange dense water with the surrounding water than a deep-convection chimney. We hasten to point out, however, that any efficiency estimate is very rough because it may change as the dynamics change. For example, we have considered the simple case of a uniform depth shelf without bottom friction, whereas GC included both a sloping bottom and bottom friction. Adding both effects does not change the behavior qualitatively, but does change the efficiency of eddy exchange. Figures 10 and 11 show the response for the standard calculation (a = 30 km, b = 10 km, W = 10 km, and B_0 = 4 × 10^{-7} m^2 s^{-3}), but over a gently sloping bottom with depth increasing uniformly from 50 m at the coast with a slope of 0.001 and with linearized bottom friction ($A_V u_z = \hat{r}u$ and $A_V v_z = \hat{r}v$ at the bottom with $\hat{r}$ = 5 × 10^{-4} m s^{-1}). The qualitative behavior is identical, but the eddies move offshore considerably faster, reducing β to about 3.5 and implying an increased eddy efficiency of α' = 0.114. Physically, the bottom slope introduces a gravitational component to the offshore acceleration of the dense water. This leads to faster offshore movement of the eddies (compare Fig. 11 with Fig. 6), hence more rapid exchange and smaller equilibrium density anomaly. Otherwise, the basic parameter dependence (9) and (11) still applies.

Finally, we have made numerous idealizations in our representation of an Arctic polynya in order to simplify the dynamics. Most notably, we have assumed a forcing whose size, shape, and strength remain fixed in time. However, numerous studies (e.g., Schumacher et al.
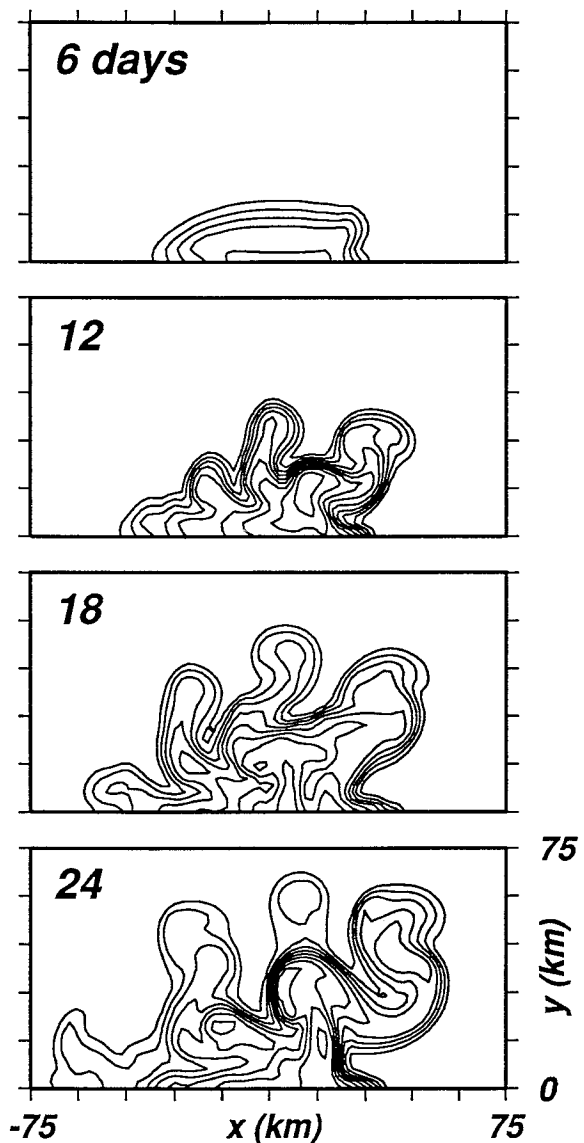

FIG. 11. As in Fig. 6 but over a uniformly sloping shelf with linear bottom friction. Contours are 0.08 to 0.8 by 0.08 kg m^{-3}.

1983; Pease 1987) have shown that coastal wind-driven polynyas are highly time-dependent features that involve repeated opening and closing of the ice cover due to synoptic wind and thermodynamic forcing. Our simple forcing is intended to represent a typical polynya size with seasonally averaged buoyancy flux, but time-dependence in both the buoyancy flux and the spatial structure of the forcing should be considered in future studies. Additional attention should be given to the gradients in ice concentration around the periphery of the coastal polynya in order to examine seasonal and synoptic variability in the forcing decay region. The effects of ambient stratification, more realistic bottom topography, and wind-driven circulation have been omitted here and should be considered as well. Nevertheless,

the present idealized treatment provides a conceptual foundation for studies that include more complicated and realistic features.

APPENDIX

Buoyancy Flux in the Forcing Decay Region

In deriving (9) and (11), we ignored the surface buoyancy flux in the forcing decay region surrounding the coastal polynya (Fig. 1). This greatly simplifies the analysis because the left-hand side of (5) can be evaluated analytically. Heuristically this simplification may be defended by noting that the eddies form within the forcing decay region, so they already contain the dense water formed there as they begin moving offshore. The equilibrium state occurs only after the eddies have exchanged water from the constant forcing region (where $B = B_0$) with ambient water, so the parameter dependence on b in (9) and (11) is sensible. However, (9) and (11) clearly fail when $b \to 0$ with $W \neq 0$; they predict $t_e = \rho_e = 0$, yet the density must change because of the buoyancy flux in the forcing decay region.

The buoyancy flux in the forcing decay region can be included in the analysis in the following manner. The total buoyancy flux is computed numerically as

$$B_T = \iint B \, dA, \quad \text{(A1)}$$

where B is given by (4). A new forcing region is now defined in which uniform buoyancy flux B_0 is imposed over a half-ellipse with axes extending beyond a and b by an amount $\hat{W}$ such that the total buoyancy flux is still B_T:

$$B_T = \iint B_0 \, dA = B_0 \frac{\pi}{2}(a + \hat{W})(b + \hat{W}). \quad \text{(A2)}$$

Solving for $\hat{W}$ yields

$$\hat{W} = \frac{a + b}{2}\left\{\left[1 + 4\left(\frac{2B_T/\pi B_0 - ab}{(a + b)^2}\right)\right]^{1/2} - 1\right\}. \quad \text{(A3)}$$

The perimeter of the new forcing region is

$$P(a, b, \hat{W}) = 2(a + \hat{W})E[1 - (b + \hat{W})^2/(a + \hat{W})^2]. \quad \text{(A4)}$$

The analysis of section 2, starting with (6), proceeds as before but with a and b replaced by $a + \hat{W}$ and $b + \hat{W}$, respectively.

All of the numerical calculations can be reinterpreted in terms of this approach to account for the entire buoyancy flux. [Of course, the numerical calculations themselves are unchanged. Only the scalings (9) and (11) and β change.] For example, the standard parameters ($B_0 = 4 \times 10^{-7}$ m^2 s^{-3}, $a = 30$ km, $b = 10$ km, $W = 10$ km, and $H = 50$ m) produce $\hat{W} = 5.1$ km, from which $\beta = 4.6$ and $\alpha' = 0.066$. So, the estimate of eddy exchange efficiency increases because the eddies are redistributing a larger total buoyancy flux in the same length of time. Otherwise, the scaled responses shown in Figs. 4 and 7 are only marginally altered, certainly not enough to question the validity of (9) and (11) as a good approximation. Presumably, the agreement would deteriorate as b becomes small relative to W, in which case a disproportionate amount of buoyancy flux would be neglected in (9) and (11). This situation has not been tested here because it is probably not important in forming dense shelf water in the Arctic.

REFERENCES

Abramowitz, M., and I. Stegun, 1965: *Handbook of Mathematical Functions.* Dover, 1046 pp.

Brickman, D., 1995: Heat flux partitioning in open-ocean convection. *J. Phys. Oceanogr., 25,* 2609–2623.

Cavalieri, D. J., and S. Martin, 1994: The contributions of Alaskan, Siberian, and Canadian coastal polynyas to the cold halocline layer of the Arctic Ocean. *J. Geophys. Res., 99,* 18 343–18 362.

Coates, M. J., G. N. Ivey, and J. R. Taylor, 1995: Unsteady, turbulent convection into a rotating, linearly stratified fluid: Modeling deep ocean convection. *J. Phys. Oceanogr., 25,* 3032–3050.

Gawarkiewicz, G., and D. C. Chapman, 1995: A numerical study of dense water formation and transport on a shallow, sloping continental shelf. *J. Geophys. Res., 100,* 4489–4507.

Haidvogel, D., J. Wilkin, and R. Young, 1991: A semi-spectral primitive equation ocean circulation model using vertical sigma and orthogonal curvilinear horizontal coordinates. *J. Comput. Phys., 94,* 151–185.

Ivey, G. N., J. R. Taylor, and M. J. Coates, 1995: Convectively driven mixed layer growth in a rotating, stratified fluid. *Deep-Sea Res., 42,* 331–349.

Jones, H., and J. Marshall, 1993: Convection with rotation in a neutral ocean: A study of open-ocean deep convection. *J. Phys. Oceanogr., 23,* 1009–1039.

Manley, T. O., and K. Hunkins, 1985: Mesoscale eddies of the Arctic Ocean. *J. Geophys. Res., 90,* 4911–4930.

Maxworthy, T., and S. Narimousa, 1994: Unsteady, turbulent convection into a homogeneous, rotating fluid, with oceanographic applications. *J. Phys. Oceanogr., 24,* 865–887.

Melling, H., 1993: The formation of a haline shelf front in wintertime in an ice-covered arctic sea. *Contin. Shelf Res., 13,* 1123–1147.

Pease, C. H., 1987: The size of wind-driven coastal polynyas. *J. Geophys. Res., 92,* 7049–7059.

Schumacher, J. D., K. Aagaard, C. H. Pease, and R. B. Tripp, 1983: Effects of a shelf polynya on flow and water properties in the northern Bering Sea. *J. Geophys. Res., 88,* 2723–2732.

Visbeck, M., J. Marshall, and H. Jones, 1996: Dynamics of isolated convective regions in the ocean. *J. Phys. Oceanogr., 26,* 1721–1934.

Whitehead, J.A., J. Marshall, and G. E. Hufford, 1996: Localized convection in rotating stratified fluid. *J. Geophys. Res., 101,* 25 705–25 722.